Origin of Amplified Spontaneous Emission Degradation in MAPbBr$_3$ Thin Films under Nanosecond-UV Laser Irradiation

Maria Luisa De Giorgi,* Titti Lippolis, Nur Fadilah Jamaludin, Cesare Soci, Annalisa Bruno, and Marco Anni

ACCESS | Metrics & More | Article Recommendations | Supporting Information

ABSTRACT: Hybrid halide perovskites have achieved excellent efficiencies and remarkable performances, not just in photovoltaic cells but also in light-emitting devices, such as light-emitting diodes, light-emitting transistors, and lasers. The lack of long-term stability is the main limitation for the commercial application of perovskite devices. While several works have investigated the origin of the degradation of perovskites in regard to solar cell applications, the operational stability of perovskites under the optical pumping regime necessary for optical gain and lasing is largely unexplored. In this work, we investigate the origin of the photodegradation of amplified spontaneous emissions (ASE) in MAPbBr$_3$ thin films under nanosecond-UV laser irradiation as a function of the pump excitation density in different environments (air and vacuum). The correlation between the observed ASE operational stability and the irradiation-induced variations in the local morphology and emission properties allowed us to demonstrate that the main process leading to ASE quenching is related to the film melting induced by localized heating. This also induces a bromine loss. Our results are relevant for the development of suitable strategies to improve the ASE values and the lasing operational stability of lead halide perovskite films.
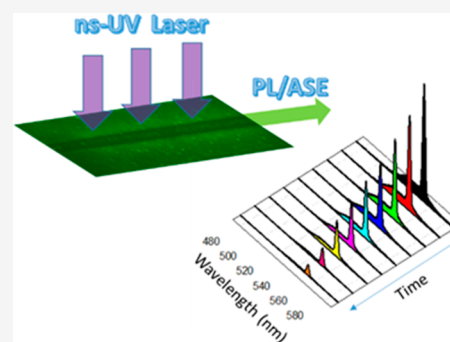
INTRODUCTION

Hybrid metal−lead halide perovskites, such as MAPbX$_3$ (where MA = methylammonium and X = Cl, Br, or I or mixed Cl/Br and Br/I systems), have recently emerged as an innovative class of photovoltaic materials with high efficiencies due to their large absorption coefficients, excellent charge mobilities, and high diffusion lengths.[1−11] Thanks to the combination of the above-mentioned outstanding properties and a low-cost deposition process from solution, inexpensive solar cells with certified power conversion efficiencies up to 25.2%[12] have been realized. In addition, it has been demonstrated that these materials also exhibit good light emission properties that allow them to be employed as active materials for light-emitting diodes (LEDs)[13−20] and light-emitting transistors.[21] Furthermore, after the first evidence of high optical gains and efficient amplified spontaneous emissions (ASE) in the bulk polycrystalline thin films of MAPbX$_3$,[22] lead halide perovskites started to be investigated as possible active materials for lasers.[19,20,22−34] In particular, ASE has been demonstrated in bulk polycrystalline thin films of organic−inorganic[22,26,28,35] and fully inorganic perovskites[36−38] as well as in perovskite nanocrystal films.[25,30−33,39] These results allowed for the realization of optically pumped perovskite lasers with different cavity geometries,[24] such as microcavity lasers,[23] distributed feedback lasers,[29,34] whispering gallery mode lasers,[27,30] and random lasers.[30]

Despite these promising properties, the possibility of a practical application to devices is actually limited, mainly due to the lack of long-term stability. Indeed, it has been demonstrated that perovskite degradation can be induced by illumination, heating, and exposure to oxygen or moisture,[28,40−47] leading to variations in the film morphology, composition, and structure and a worsening of the performance of the devices. A deep understanding of the physical and chemical processes leading to the degradation of the active thin films is thus necessary in order to determine the best strategy to develop materials and devices with improved operational stabilities. To date, most of the experiments on perovskite degradation have been focused on solar cells.[48−53]

The possible use of metal halide perovskites in light-emitting devices has also stimulated experiments regarding the stability of the photoluminescence (PL), which highlighted the importance of several factors, such as the wavelength[43] and
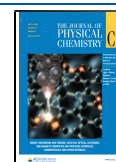
the time regime (from CW to fs laser pulses) of the excitation as well as the sample environment.[42,44,46] Considering the strong optical pumping regime necessary to reach the population inversion conditions necessary to achieve optical gain and lasing, the active material stability is expected to be particularly critical in the working conditions of a laser device. Despite this, the investigation of the ASE and the lasing operational stability is limited to the characterization of the time scale of the intensity decrease during continuous pumping[22,54−57] and the development of possible approaches to increase it.[28,33,39] However, the origin of the active material degradation that leads to the ASE intensity decrease is to date completely unexplored.

In this paper, we investigate this issue for the first time by quantitatively studying the ASE operational stability of MAPbBr$_3$ thin films as a function of the pump excitation density and the environment. We demonstrate that the ASE threshold is independent of the environment but that at any excitation density above the threshold the ASE intensity is higher in air than in a vacuum. We also show, by PL mapping and SEM, that the ASE degradation in a vacuum is mainly related to a variation in the film morphology in the region of the maximum pump intensity, leading to a localized PL quenching for excitation densities up to 3× the ASE threshold. At excitation densities of at least 4.5× the ASE threshold, localized film melting takes place that leads to a fast ASE intensity decrease and the photodegradation of the active material, which in turn leads to bromine loss. We finally demonstrate that the film pumping in air beyond the degradation processes is qualitatively similar to that in a vacuum, allowing for an improvement of the emission properties ascribed to oxygen-induced defect passivation and leading to an ASE intensity recovery and overall better intensity stability than in a vacuum.

These results show that the main element causing the degradation of MAPbBr$_3$ is the localized heating caused by the strong optical pumping and suggests that heat dissipation optimization is a critical feature for the development of optically pumped perovskite lasers with high operational stabilities.

EXPERIMENTAL SECTION

Sample Fabrication. Quartz substrates were first sequentially cleaned in a decon soap with deionized water and isopropanol for 15 min each. The substrates were then blow-dried with N$_2$ and ozone-treated for 30 min prior to spin-coating. Next, 0.3−0.5 M MAPbBr$_3$ perovskite solutions were prepared by dissolving MABr and PbBr$_2$ in a DMF:DMSO cosolvent (25% DMSO) at a ratio of 1.05:1. The films were fabricated using a widely reported solvent engineering process, where 40 μL of the perovskite solution was spin-coated onto the substrate at 5000 rpm for 30 s, followed by toluene dripping 5 s later. The films were then dried under vacuum for 30 min before any measurements were made. The obtained films had a thickness of about 120 nm.

Photoluminescence and Amplified Spontaneous Emission. The photoluminescence properties were explored by pumping the films with a nitrogen laser at 337 nm by delivering 3 ns pulses with a repetition rate of 10 Hz. The pump beam was focused onto the sample surface by a cylindrical lens in a rectangular stripe with a length of about 4 mm and width of 80 μm, which was characterized by a transverse Gaussian profile with a superimposed peak

corresponding to its maximum (Figure S1). The emission, which was waveguided by the active film, was collected from the sample edge at the corresponding end of the excitation stripe by means of an optical fiber coupled to a spectrometer (ACTON SpectraPro-750) equipped with a CCD (Andor). The spectral resolution was about 0.5 nm. Measurements were performed in a vacuum (at a pressure of about 10^{-2} mbar) and in air (at atmospheric pressure) at room temperature.

Degradation Experiments. The samples were photo-pumped at normal incidence with the N$_2$ laser at different pump energy densities (about 1.5, 3, 4.5, and 6× the ASE threshold) for a maximum of 8 min (4800 pulses). The PL spectra were recorded every 2 s in order to investigate the degradation dynamics.

Scanning Electron Microscopy and Energy-Dispersive X-ray Spectroscopy. Scanning electron microscopy (SEM) images were collected using a high-vacuum tungsten filament microscope (JEOL JSM-6480LV, dedicated software: SEM/JSM 5000) with a working bias of 5 kV. Elemental distribution was inferred through energy-dispersive X-ray (EDX) analyses (IXRF analyzer 500, dedicated software: EDS 2008) with a working bias of 20 kV.

Fluorescence Microscopy. Fluorescence maps of the areas previously pumped with the N$_2$ laser were recorded by means of a Nikon Eclipse C1 inverted microscope by exciting the samples with a Hg lamp in the range of 480 ± 15 nm. The PL was collected in a backscattering configuration and detected in the range of 530 ± 20 nm.

RESULTS AND DISCUSSION

Photoluminescence Excitation Density Dependence. As a first step, we characterized the emission properties of the film by measuring the excitation density dependence of the PL spectra both in a vacuum and in ambient conditions. In both cases, a spontaneous emission (SE) band centered at about 530 nm was observed at low excitation densities (Figure 1a and b), while a clear ASE band appeared at 553 nm with a threshold of 0.22 mJ cm^{-2} and a strongly increasing peak intensity above the threshold (Figure 1c). The excitation density dependence of the ASE intensity allowed us to observe that, despite the identical thresholds in a vacuum and in air, the ASE intensity shows a stronger increase with the excitation density in air than in a vacuum. This is evidenced by an intensity at 1.30 mJ cm^{-2} that is about 2× larger in air than in a vacuum. A similar effect was also observed for the excitation density dependence of the SE peak intensity at about 530 nm (Figure S2), showing that the SE intensity in air was about 1.2× higher than in a vacuum.

ASE Intensity Stability as a Function of the Excitation Density. The emission intensity stability during continuous laser pumping was investigated at four different excitation densities above the ASE threshold (namely 1.5, 3.0, 4.5, and 6.0× the ASE threshold excitation density) by measuring the PL spectra every 2 s (every 20 laser pulses) under continuous pumping along a time interval of 8 min. The SE peak intensity (Figure S3) does not decrease during continuous laser pumping even at the highest excitation density, both in a vacuum and in air. By contrast, the ASE peak intensity (Figure 2) shows a clear intensity variation with time that depends on both the excitation density and the environment.

At the lowest excitation density of 0.34 mJ cm^{-2} (1.5× above the ASE threshold), the ASE is stable in both a vacuum and air. As the excitation density increases, the ASE intensity
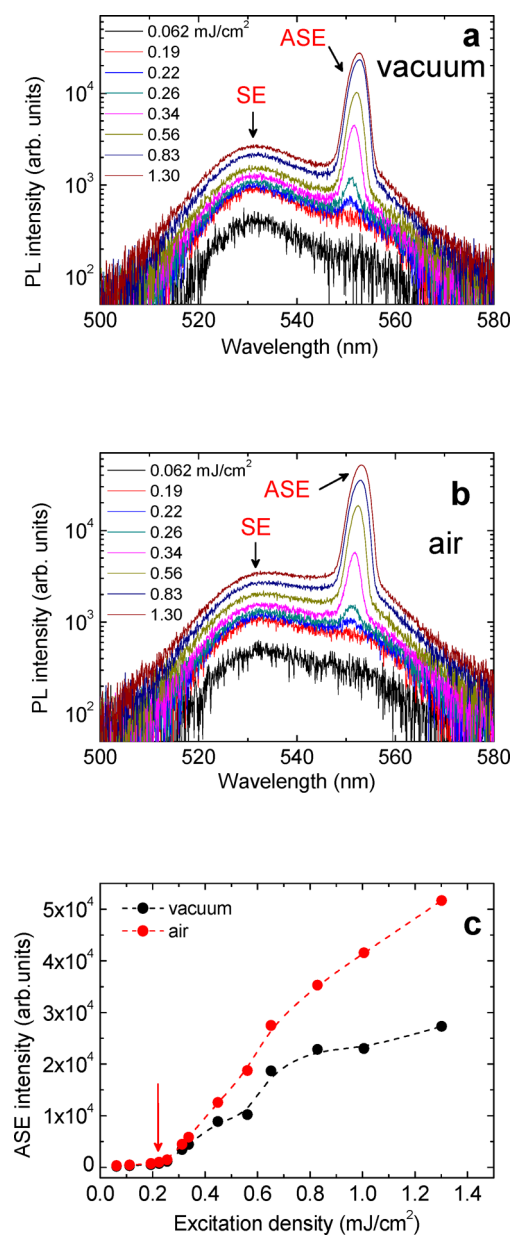
Figure 1. Excitation density dependence of the PL spectra of the sample both in (a) a vacuum and (b) air. (c) The excitation density dependence of the ASE peak intensity (the lines are guides for the eyes). The arrow indicates the ASE threshold.

Figure 2. Normalized ASE peak intensity as a function of time during continuous laser pumping at different excitation densities in (a) a vacuum and (b) air.

decreases with trends and times that depend on the energy density and the environment.

Sample irradiation in a vacuum at an excitation density of 0.65 mJ cm^{-2} (3× above the ASE threshold) leads to a progressive decrease of the ASE intensity (Figure 2a). When the excitation density was further increased to 1.01 mJ cm^{-2} (4.5× above the ASE threshold), two ASE degradation regimes were observed; the first dominates in the initial 80 s and leads to the loss of about 40% of the initial intensity, and a second slower one at higher irradiation times leads to the loss of about 10% of the intensity in the remaining 400 s. At the maximum excitation density of 1.30 mJ cm^{-2} (6× above the ASE threshold), the fast process becomes even faster and leads to the loss of about 50% of the intensity, which was followed by a slower decay. Overall, the ASE degradation becomes stronger as the irradiation energy density increases, as evidenced by the
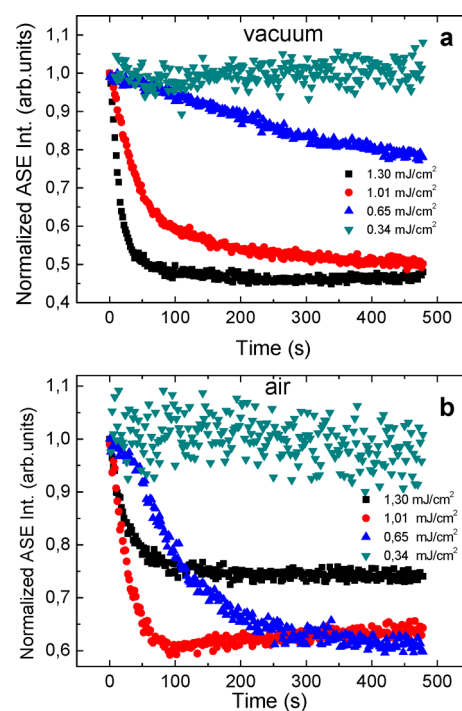
progressive decrease of the relative final (remnant) ASE intensity.

When the sample was irradiated in air at 0.65 mJ cm^{-2}, we observed an ASE decay faster than that in a vacuum. The presence of the two temporal regimes was instead observed under irradiation at 1.01 mJ cm^{-2}, but the initial fast degradation was unexpectedly followed by an intensity recovery that dominated for irradiation times higher than about 100 s and leads to a final relative intensity higher than the one at 0.65 mJ cm^{-2}. Finally, at the maximum irradiation energy density the initial fast-intensity decay was present in the first 60 s and was then followed by an almost constant intensity, with a further clear increase of the final relative intensity.

In order to quantitatively analyze the previous results, the ASE intensity decays in Figure 2 have been fitted with the function

$$I(t) = A \exp\left(-\frac{t}{\tau_{ASE}}\right) + I_0$$

(1)

where τ_{ASE} and I_0 represent the photostability mean lifetime and the remnant ASE emission of the MAPbBr$_3$ films, respectively. The best-fit values for these parameters are summarized in Table 1.

By comparing the obtained values of τ_{ASE}, one can notice that while in a vacuum the degradation rate progressively increases with the excitation density, in air the initial fast degradation is followed by a slowing of the process when the excitation density increases from 1.01 to 1.30 mJ cm^{-2}. Moreover, by comparing the curves at 1.30 and 0.65 mJ cm^{-2} in air, one can notice that even if the film degrades more rapidly at 1.30 mJ cm^{-2} than at 0.65 mJ cm^{-2} (the photostability mean lifetime τ_{ASE} is lower), the remnant ASE emission grows with an increase in the excitation density due

Table 1. Best-Fit Parameters for the Normalized Degradation Curves at Different Excitation Densities in a Vacuum and in Air

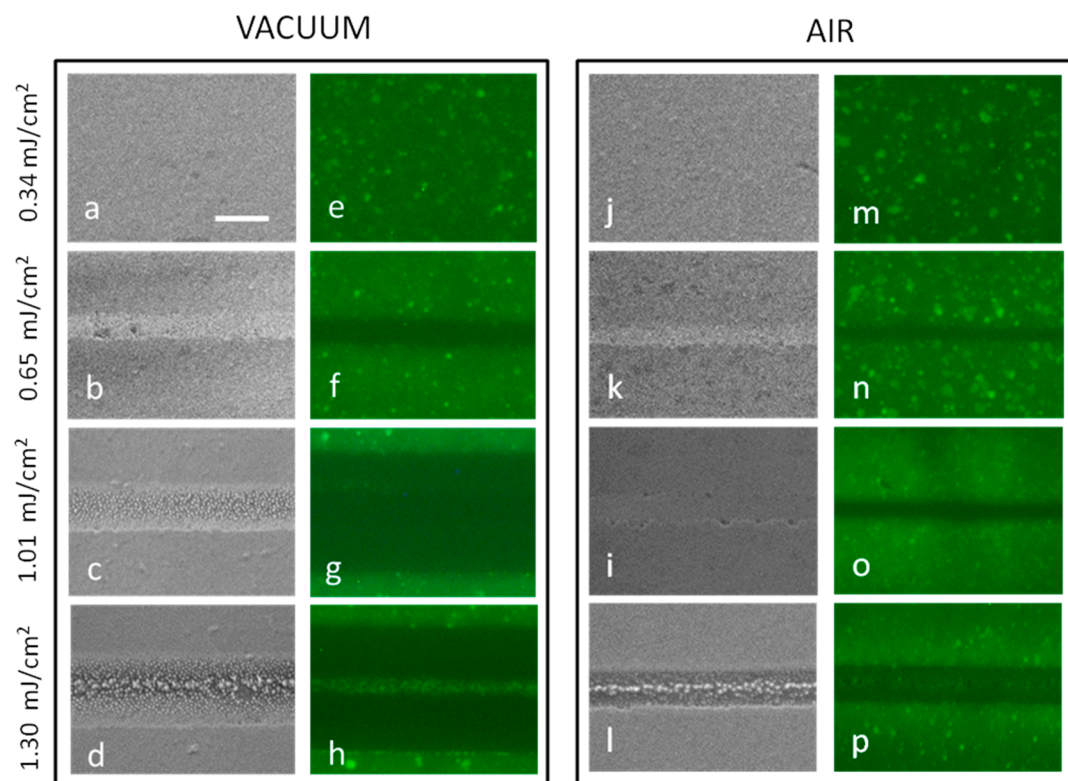| excitation density (mJ cm^{-2})	vacuum		air	
	I_0	τ_{ASE} (s)	I_0	τ_{ASE} (s)
0.34	0.915 ± 0.002		0.91 ± 0.04	
0.65	0.60 ± 0.02	575 ± 50	0.599 ± 0.002	112 ± 3
1.01	0.5179 ± 0.0011	52.6 ± 0.9	0.6239 ± 0.0010	26.7 ± 0.8
1.30	0.4669 ± 0.0007	17.3 ± 0.3	0.7443 ± 0.006	30.1 ± 0.8

Figure 3. Comparison of 21 × 15.8 μm^2 top-view scanning electron microscopy (SEM) images (a−d and i−l) and 20 × 15 μm^2 fluorescence maps (e−h and m−p) of the irradiated areas following continuous laser pumping for 8 min at different excitation densities in a vacuum (left) and in air (right). The scale bar is 5 μm.

to some processes that sustain the amplified spontaneous emission and overcome the degradation in air. This process will be investigated in the following section.

Overall, our results highlight that SE emissions do not decrease regardless of the excitation energy, whereas laser pumping induces ASE degradation for excitation densities higher than 1.5× the threshold. However, after an initial quick decrease the ASE peak remains almost stable for longer irradiation times (Figure S4), and the growth of the remnant ASE intensity is more rapid in air than in a vacuum (Table S1).

Morphological and Local Emission Laser-Induced Effects. In order to investigate the processes that cause the decrease in the ASE intensity and to explain the observed excitation densities and environment dependence, we investigated the effects of irradiation on the film morphology and the local emission properties by scanning electron and photoluminescence mapping microscopy (Figure 3) at the end of each irradiation cycle.

Irradiating the film at 0.34 mJ cm^{-2} in a vacuum (Figure 3a) did not lead to any morphological variations, which is consistent with the stable value of the ASE intensity. A clear track corresponds to the most intense part of the laser beam profile, where the sample at a higher laser density becomes

wider as the excitation density increases (Figure 3b−d). In particular, as detected from SEM micrographs, the laser footprint width when the sample is irradiated in a vacuum progressively increases from about 2 μm to about 7 μm when the excitation density is increased from 0.65 to 1.30 mJ cm^{-2} (Figure 4a). Moreover, irradiation at an excitation density above 1.01 mJ cm^{-2} also causes a granular morphology in the central region of the pump stripe, suggesting that the energy transferred from the laser beam to the MAPbBr$_3$ film is high enough to induce melting. When the film is irradiated in air, the results (Figure 3i−l) are qualitatively similar, but the widths of the footprints induced by the laser are smaller than those observed for excitation in vacuum (Figure 4a).

Concerning the PL maps after the irradiation in a vacuum, we observed no PL intensity variations at an excitation density of 0.34 mJ cm^{-2} (Figure 3e), while clearly localized PL quenching was observed at higher excitation densities (Figure 3f−h). The width of the region showing the PL quenching progressively increases with the excitation density (Figure 4a), and at the two higher excitation densities they are much larger than the width of the laser footprints observed in the SEM images. We also observed that a clear high-intensity line can be seen in the middle of the quenched area exposed at the
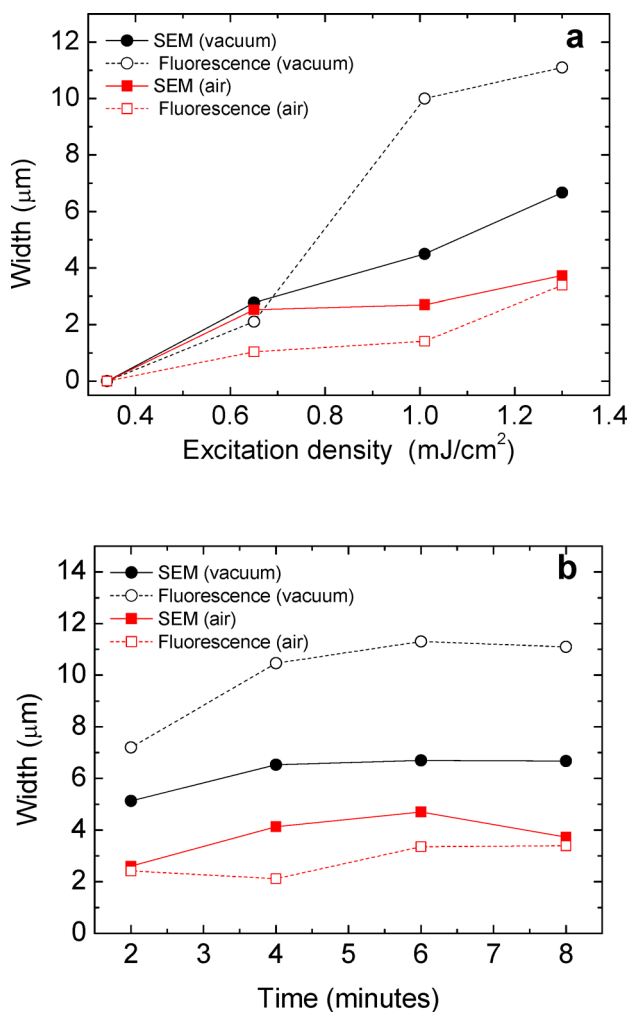
Figure 4. Footprint width in a vacuum and in air as detected from SEM images and fluorescence maps as a function (a) of the excitation density under continuous laser pumping and (b) the time at 1.30 mJ cm^{-2}.

maximum excitation density (Figure 3h), suggesting that the recrystallization after melting leads to a photoluminescent perovskite structure.

For the sample irradiated in air, we observed similar results (Figure 3m–p). However, the region containing the PL quenching is much thinner than that in a vacuum and also than the laser footprint visible in the SEM images. These results demonstrate that laser exposure in a vacuum leads to a local variation of the film properties, resulting in a PL quenching that is also present in regions with unmodified morphologies. When the measurements are performed in air, the local morphology variations induced by the irradiation of the laser do not necessarily induce PL quenching.

In order to rationalize the previous results, we estimated the local temperature increase due to the heat induced by the laser light absorption. In our experimental conditions, the increase of surface temperature after the laser pulse is given by

$$\Delta T = \frac{\alpha D}{\rho c} \tag{2}$$

where D is the excitation energy density of the laser and α, ρ, and c are the absorption coefficient, the mass density, and the specific heat of the sample, respectively.

By analyzing the surface irradiated at the average excitation energy density over the total laser spot of 1.30 mJ cm^{-2} through electron microscopy, we found that the morphologically modified area (Figure 3d) corresponded to the central part of the beam that is characterized by a higher local excitation energy density. By considering the spatial intensity distribution of the beam (Figure S1), we evaluated the excitation energy density in the center of a laser beam of about 2.6 mJ cm^{-2}, leading to an estimated temperature increase of about 270 °C; this is well above the melting point of MaPbBr$_3$ (>200 °C).[58] The estimated temperature increase is an upper limit, as part of the absorbed energy is radiatively dissipated. This estimation supports the attribution of the observed morphology modifications to localized melting followed by rapid resolidification. The solidification occurs with the growth of small spherical clusters as shown in Figure S5, which shows the details of the central part of the irradiated area that is characterized by the typical morphology of a melted layer and is successively resolidified. However, in the side regions the temperature that is reached is not high enough to induce melting but is instead sufficient in order to modify the morphology and photoluminescence of the film (see the fluorescence maps in Figure 3). In particular, the observation that in a vacuum the PL is quenched in a region larger than the one in which the morphology changes shows evidence of the formation of nonradiative defects, which are probably related to the heating of the local film. On the contrary, in air the PL quenching region is smaller than that observed in the SEM images, and the PL intensity outside the melted region is enhanced. This suggests that the local heating, when combined with oxygen, allows for the film recrystallization that enhances the PL quantum yield. This explains the progressive reduction in the ASE relative quenching as the excitation density increases. Lastly, in the lateral sides heated by the Gaussian beam tails neither morphological nor emission degradation is provoked. This explanation is also consistent with the absence of a decrease in the SE intensity during illumination. Indeed, the SE mainly comes from the side of the pump stripe, where the excitation density is very low (less than the ASE threshold) and degradation does not take place.

Analogous considerations can be made for the irradiation at 1.01 mJ cm^{-2} (Figure 3c). The energy density in the central region of the footprint leads to a temperature increase of about 210 °C, which is above the melting point of the film. In contrast, at 0.65 mJ cm^{-2} (Figure 3b) the temperature increase (about 135 °C) is not enough to induce melting in the film, even if the evident morphological and emission variations are still visible. At 0.34 mJ cm^{-2} (Figure 3a and e), the energy density is too low to induce any type of degradation in the irradiated film.

From the analysis of the ASE peak dynamics in a vacuum on the basis of the estimated temperatures in the irradiated areas, one can notice that when the irradiation induces melting in the film the ASE degradation becomes faster and the remnant ASE emission decreases. In contrast, no ASE degradation is present at the lowest used energy density where no modifications are detected by microscopy.

In order to understand the different behavior in air, and in particular the lower values of the laser footprint widths (Figure 3i, k, l, n–p and the graph in Figure 4a), we investigated the possible role of a more efficient heat dissipation that leads to lower values of the local temperature.
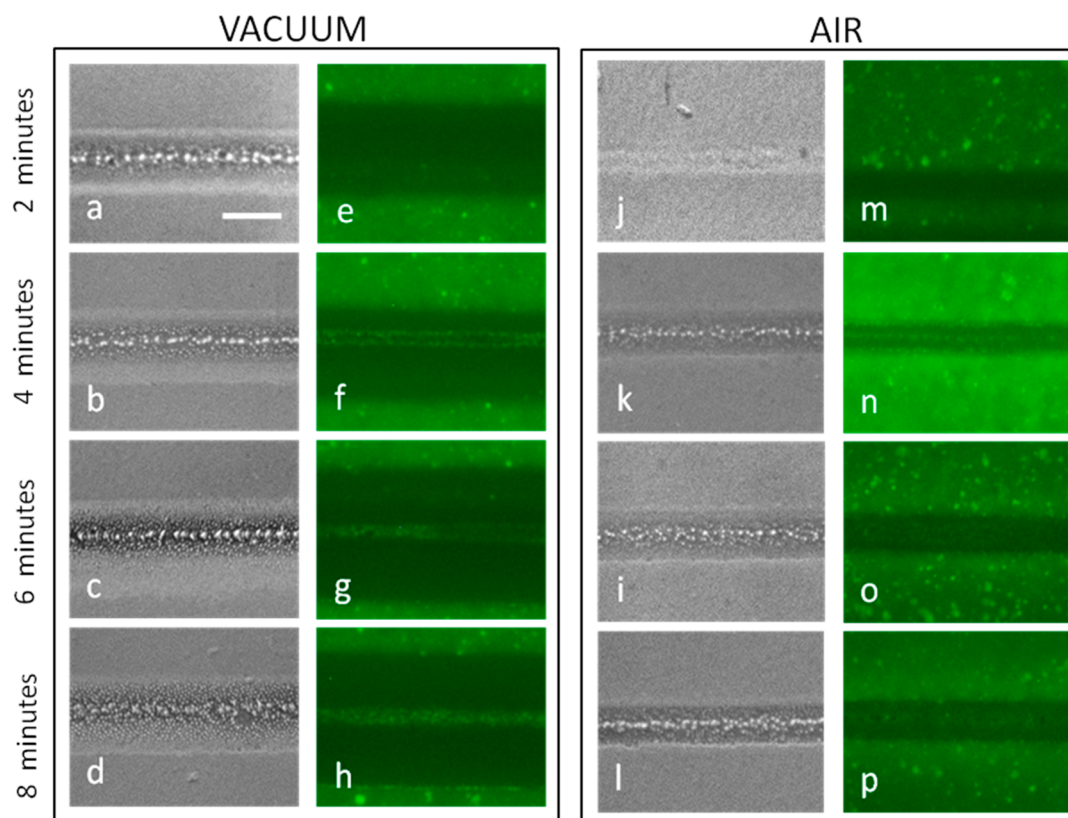
Figure 5. Comparison of the 21 × 15.8 μm^2 top-view scanning electron microscopy (SEM) images (a−d and i−l) and 20 × 15 μm^2 fluorescence maps (e−h and m−p) of the irradiated areas at 1.30 mJ cm^{-2} excitation density after different time lapses in (left) a vacuum and (right) air. The scale bar is 5 μm.

Heat loss from a film can generally take place via different processes that would induce different reductions of the film surface temperature in air compared to irradiation in a vacuum. In our experimental conditions, at atmospheric pressure convection is expected to be the main cause of the reduction of the temperature increase induced in the film by laser irradiation in air. Indeed, heat loss by thermal radiation and direct energy absorption by the ambient energy from the laser radiation, which lowers the energy impinging onto the surface, can be ignored. Furthermore, because of the very different thermal conductivity values of MAPbBr$_3$, air, and glass substrates ($k_{MAPbBr3}$ = 44 × 10^{-4} W K^{-1} cm^{-1}, k_{air} = 2.6 × 10^{-4} W K^{-1} cm^{-1}, k_{glass} = 10^{-2} W K^{-1} cm^{-1}), the contribution of heat flow via heat conduction can be considered negligible.

Regardless, it is important to observe that although a reduced local temperature increase would actually lead to a smaller width of the degraded region, this feature alone cannot fully explain the observed ASE degradation dynamics. Decreased heating would actually lead to a degradation dynamic variation with the excitation density similar to that in a vacuum, and eventually one with a slower degradation and a higher remnant intensity. Instead, our results at 1.01 mJ cm^{-2} clearly show the interplay between a fast degradation, ascribed to the film melting, and a second process leading to an increase in the ASE intensity. This strongly suggests that the reduced heating in air is not the main effect that determines the differences between the degradation dynamics in air and in a vacuum.

Compositional Laser-Induced Effects. In order to probe the differences between the active film degradation processes in air and in a vacuum, we also performed elemental analyses by means of EDX (energy-dispersive X-ray) investigations over the surface (Figure S6). The average relative atomic ratio of Br to Pb (Br:Pb) in the nonmelted areas of the film is equal to 3.44 ± 0.13, while in the laser melted regions it is equal to 1.42 ± 0.18 in a vacuum and 0.88 ± 0.13 in air. Thus, in the nonmelted regions the ratio is compatible with the stoichiometry of MAPbBr$_3$, whereas irradiation induces a clear loss of bromine in the melted areas; this loss is much higher in air than in a vacuum.

In previous works it has been shown that the MAPbBr$_3$ degradation under light exposure or at high temperature is due to the following reaction[52]

$$MAPbBr_3 \rightarrow PbBr_2 + CH_3NH_2 + HBr \qquad (3)$$

which represents an irreversible decomposition of MAPbBr$_3$ due to the loss of Br in the form of gaseous HBr. Since the Br:Pb value deviates from the stoichiometric ratio only in the melted areas, we can state that in our films in the degradation processes the thermally activated reactions due to the increase in temperature are much more relevant than photodecomposition due to the direct interaction of the material with the laser beam. The stronger bromine loss in air is consistent with previous investigations in the literature, showing the possible PbBr$_2$ decomposition in the presence of oxygen and under laser irradiation that leads to the formation of PbO and volatile Br$_2$.[47]

The evidence of the ASE intensity recovery only during irradiation in air clearly shows the presence of a second process in addition to photodegradation that improves the emission properties. This result is consistent with the observed increase in the PL intensity in the MAPbI$_3$ thin films that were

irradiated in air, which is ascribed to the formation of highly reactive superoxide O_2^-. These reactive species could enhance the decomposition reaction of $MAPbBr_3$, leading to the formation of methylamine, water, $PbBr_2$, and Br_2.[59] However, on the other hand they could result in defect passivation and PL enhancement.[60,61]

Considering the clear correlation between the local melting of the films and the ASE quenching, it is reasonable to assume that the observed remnant ASE emission mainly comes from the nonmolten regions of the films. This suggests that the enhancement of the remnant ASE emission observed in air could be attributed to oxygen-induced defect passivation in the lateral regions of the laser footprint. This attribution explains both the increase of the remnant normalized ASE emission in air from 0.65 to 1.30 mJ cm^{-2} as well as the higher ASE lifetime at 1.30 mJ cm^{-2} compared to that evaluated at 1.01 J cm^{-2}.

Concerning the origin of the passivated defects, we observed that the main nonradiative recombination centers in lead halide perovskites films are related to the surface or bulk defect states, both of which are of chemical and structural (grain boundaries) origin. In particular, in $MAPbBr_3$ the most probable cause of quenching could be due to the presence of Br vacancies that may act as nonradiative recombination centers. During irradiation in air, reactive oxygen species could passivate the halide vacancies and deactivate the trapping sites responsible for the nonradiative charge recombination. Moreover, oxygen-assisted recrystallization has been also proposed in the literature[50] and results in similar effects. Therefore, the ASE enhancement observed during the irradiation in air may be due to either the passivation of the surface and bulk defects or an improved crystallinity with oxygen related to the photoinduced reaction.

Degradation Dynamics. As a final point, in order to further correlate the faster ASE degradation dynamics to the film morphological degradation we also performed SEM measurements and fluorescence mapping (Figure 5) at the intermediate steps of the irradiation (2, 4, 6, and 8 min) at the highest used excitation density. In the SEM micrographs, the presence of film melting in the central part of the pump stripe is quite evident within 2 min in a vacuum and within 4 min in air. From there, the damage and the width of the footprints increase very slowly and finally are almost constant (Figure 4b).

From the ASE behavior, we found that the degradation occurs mainly within the first minute (< 600 pulses); in particular, the ASE intensity decreases very rapidly in the first minute (Figure S7) and is characterized by τ_{ASE} values of about 17 s in a vacuum and 30 s in air. The higher value of τ_{ASE} in air than in a vacuum is in accordance with the higher irradiation time necessary to observe the film melting morphological effects, which is likely due to a smaller local temperature increase. These results are consistent with the attribution of the faster ASE degradation dynamics to the film melting. Indeed, the remnant ASE emission in air is higher than that in vacuum because the damaged area is thinner and the region contributing to the emission is larger.

CONCLUSIONS

In summary, we have demonstrated that laser irradiation of $MAPbBr_3$ thin films with nanosecond pulses at excitation densities higher than the ASE threshold does not affect the SE, although it can result in ASE degradation and local variations of both the film morphology and the PL intensity. For energy densities as low as 1.5× the threshold, the ASE intensity and the film morphology are stable over continuous illumination for over 500 s. Instead, by increasing the excitation density both localized morphological variations corresponding to the central part of the pump stripe and a decrease in the ASE intensity are observed. At the highest used values of the average energy density (up to 4.5 and 6× the ASE threshold), the energy absorbed by the material, which corresponds to the maximum intensity of the beam, is high enough to melt off the film. The morphology of these areas appears deeply modified due to the melting and subsequent resolidification of the material. This thermal process is responsible for the fast ASE degradation of the samples, with a characteristic time faster than 1 min, and for the slower ASE intensity variations observed for longer irradiation times. We also showed that the ASE properties (intensity and stability) are improved when the film is pumped in air, suggesting that the interaction with oxygen has overall positive effects on the emission properties of $MAPbBr_3$. In general, our results show that the main issue to be addressed in order to improve the ASE operational stability of perovskite thin films pumped in the nanosecond regime is heat dissipation, rather than encapsulation in order to prevent chemical decomposition. This issue could be addressed by, for example, pumping the films as close as possible to the absorption peak, thus decreasing the heating due to the energy difference between the pump photons and the emitted ones, or by improving the heat conductivity of the substrates. Lastly, the different contributions to the total emission from the spontaneous and the stimulated emissions and the behavior of the stimulated emissions that results from the interplay between the degradation ascribed to the film melting at the center of the laser spot and the intensity increase in air attributed to the oxygen-induced defect passivation in the lateral regions of the laser footprint are due to the inhomogeneity of the laser intensity profile. A uniform distribution of the local excitation energy density will probably allow for better control of the emission properties.

ASSOCIATED CONTENT

ⓈI Supporting Information

The Supporting Information is available free of charge at https://pubs.acs.org/doi/10.1021/acs.jpcc.0c02331.

Evaluation of the local temperature increase due to laser irradiation, the laser intensity profile, the excitation density dependence of the SE peak intensity, the normalized SE peak intensity as a function of time during continuous laser pumping, the ASE peak intensity as a function of time, detailed SEM image of a melted area, EDX spectra, the normalized ASE peak intensity as a function of time, and fitting parameters from degradation curves at different excitation densities in vacuum and air (PDF)

AUTHOR INFORMATION

Corresponding Author

Maria Luisa De Giorgi − *Dipartimento di Matematica e Fisica "Ennio De Giorgi", Università of Salento, 73100 Lecce, Italy;* ⓞ orcid.org/0000-0002-3774-6477;
Email: marialuisa.degiorgi@unisalento.it

Authors

Titti Lippolis − *Dipartimento di Matematica e Fisica "Ennio De Giorgi", Università of Salento, 73100 Lecce, Italy*

Nur Fadilah Jamaludin − *Energy Research Institute @ NTU (ERI@N), Nanyang Technological University, 637553, Singapore*

Cesare Soci − *Division of Physics and Applied Physics, School of Physical and Mathematical Sciences, Nanyang Technological University, 637371, Singapore;* ⓞ orcid.org/0000-0002-0149-9128

Annalisa Bruno − *Energy Research Institute @ NTU (ERI@N), Nanyang Technological University, 637553, Singapore;* ⓞ orcid.org/0000-0002-6963-1682

Marco Anni − *Dipartimento di Matematica e Fisica "Ennio De Giorgi", Università of Salento, 73100 Lecce, Italy;* ⓞ orcid.org/0000-0002-1651-0166

Complete contact information is available at:
https://pubs.acs.org/10.1021/acs.jpcc.0c02331

Notes

The authors declare no competing financial interest.

■ REFERENCES

(1) Snaith, H. J. Present Status and Future Prospects of Perovskite Photovoltaics. *Nat. Mater.* **2018**, *17*, 372−376.

(2) Stranks, S. D.; Snaith, H. J. Metal-Halide Perovskites for Photovoltaic and Light-Emitting Devices. *Nat. Nanotechnol.* **2015**, *10*, 391−402.

(3) Johnston, M. B.; Herz, L. M. Hybrid Perovskites for Photovoltaics: Charge-Carrier Recombination, Diffusion, and Radiative Efficiencies. *Acc. Chem. Res.* **2016**, *49*, 146−154.

(4) Brenner, T. M.; Egger, D. A.; Kronik, L.; Hodes, G.; Cahen, D. Hybrid Organic− Inorganic Perovskites: Low-Cost Semiconductors with Intriguing Charge-Transport Properties. *Nat. Rev. Mater.* **2016**, *1*, 15007.

(5) Gratzel, M. The Light and Shade of Perovskite Solar Cells. *Nat. Mater.* **2014**, *13*, 838−842.

(6) Green, M. A.; Ho-Baillie, A.; Snaith, H. J. The Emergence of Perovskite Solar Cells. *Nat. Photonics* **2014**, *8*, 506−514.

(7) Park, N. G. Organometal Perovskite Light Absorbers toward a 20% Efficiency Low-Cost Solid-State Mesoscopic Solar Cell. *J. Phys. Chem. Lett.* **2013**, *4*, 2423−2429.

(8) Zhou, H.; Chen, Q.; Li, G.; Luo, S.; Song, T.; Duan, H.-S.; Hong, Z.; You, J.; Liu, Y.; Yang, Y. Interface Engineering of Highly Efficient Perovskite Solar Cells. *Science* **2014**, *345*, 542−546.

(9) Nie, W.; Tsai, H.; Asadpour, R.; Blancon, J.-C.; Neukirch, A. J.; Gupta, G.; Crochet, J. J.; Chhowalla, M.; Tretiak, S.; Alam, M. A.; et al. High-Efficiency Solution-Processed Perovskite Solar Cells with Millimeter-Scale Grains. *Science* **2015**, *347*, 522−525.

(10) Dong, Q.; Fang, Y.; Shao, Y.; Mulligan, P.; Qiu, J.; Cao, L.; Huang, J. Solar cells. Electron-Hole Diffusion Lengths > 175 μm in Solution-Grown $CH_3NH_3PbI_3$ Single Crystals. *Science* **2015**, *347*, 967−970.

(11) Herz, L. M. Charge-Carrier Mobilities in Metal Halide Perovskites: Fundamental Mechanisms and Limits. *ACS Energy Lett.* **2017**, *2*, 1539−1548.

(12) National Renewable Energy Laboratory. *Research Cell Record Efficiency Chart.* https://www.nrel.gov/pv/cell-efficiency.html (accessed 2020-03-03).

(13) Kumawat, N. K.; Liu, X.-K.; Kabra, D.; Gao, F. Blue Perovskite Light-Emitting Diodes: Progress, Challenges and Future Directions. *Nanoscale* **2019**, *11*, 2109−2120.

(14) Stranks, S. D.; Burlakov, V. M.; Leijtens, T.; Ball, J. M.; Goriely, A.; Snaith, H. J. Recombination Kinetics in Organic-Inorganic Perovskites: Excitons, Free Charge, and Subgap States. *Phys. Rev. Appl.* **2014**, *2*, 034007.

(15) Cho, H.; Jeong, S. H.; Park, M. H.; Kim, Y. H.; Wolf, C.; Lee, C. L.; Heo, J. H.; Sadhanala, A.; Myoung, N. S.; Yoo, S.; Im, S. H.; Friend, R. H.; Lee, T. W. Overcoming the Electroluminescence Efficiency Limitations of Perovskite Light-Emitting Diodes. *Science* **2015**, *350*, 1222−1225.

(16) Lin, K.; Xing, J.; Quan, L. N.; de Arquer, F. P. G.; Gong, X.; Lu, J.; Xie, L.; Zhao, W.; Zhang, D.; Yan, C.; et al. Perovskite Light-Emitting Diodes with External Quantum Efficiency Exceeding 20 per Cent. *Nature* **2018**, *562*, 245−248.

(17) Cao, Y.; Wang, N.; Tian, H.; Guo, J.; Wei, Y.; Chen, H.; Miao, Y.; Zou, W.; Pan, K.; He, Y.; et al. Perovskite Light-Emitting Diodes Based on Spontaneously Formed Submicrometre-Scale Structures. *Nature* **2018**, *562*, 249−253.

(18) Van Le, Q.; Jang, H. W.; Kim, S. Y. Recent Advances toward High-Efficiency Halide Perovskite Light-Emitting Diodes: Review and Perspective. *Small Methods* **2018**, *2*, 1700419.

(19) Veldhuis, S. A.; Boix, P. P.; Yantara, N.; Li, M.; Sum, T. C.; Mathews, N.; Mhaisalkar, S. G. Perovskite Materials for Light-Emitting Diodes and Lasers. *Adv. Mater.* **2016**, *28*, 6804−6834.

(20) Sutherland, B. R.; Sargent, E. H. Perovskite Photonic Sources. *Nat. Photonics* **2016**, *10*, 295−302.

(21) Chin, X. Y.; Cortecchia, D.; Yin, J.; Bruno, A.; Soci, C. Lead Iodide Perovskite Light-Emitting Field-Effect Transistor. *Nat. Commun.* **2015**, *6*, 7383.

(22) Xing, G.; Mathews, N.; Lim, S. S.; Yantara, N.; Liu, X.; Sabba, D.; Gratzel, M.; Mhaisalkar, S.; Sum, T. C. Low-Temperature Solution-Processed Wavelength-Tunable Perovskites for Lasing. *Nat. Mater.* **2014**, *13*, 476−480.

(23) Deschler, F.; Price, M.; Pathak, S.; Klintberg, L. E.; Jarausch, D. D.; Higler, R.; Huttner, S.; Leijtens, T.; Stranks, S. D.; Snaith, H. J.; et al. High Photoluminescence Efficiency and Optically Pumped Lasing in Solution-Processed Mixed Halide Perovskite Semiconductors. *J. Phys. Chem. Lett.* **2014**, *5*, 1421−1426.

(24) De Giorgi, M. L.; Anni, M. Amplified Spontaneous Emission and Lasing in Lead Halide Perovskites: State of the Art and Perspectives. *Appl. Sci.* **2019**, *9*, 4591−4621.

(25) Balena, A.; Perulli, A.; Fernandez, M.; De Giorgi, M. L.; Nedelcu, G.; Kovalenko, M. V.; Anni, M. Temperature Dependence of the Amplified Spontaneous Emission from $CsPbBr_3$ Nanocrystal Thin Films. *J. Phys. Chem. C* **2018**, *122*, 5813−5819.

(26) Stranks, S. D.; Wood, S. M.; Wojciechowski, K.; Deschler, F.; Saliba, M.; Khandelwal, H.; Patel, J. B.; Elston, S. J.; Herz, L. M.; Johnston, M. B.; et al. Enhanced Amplified Spontaneous Emission in Perovskites Using a Flexible Cholesteric Liquid Crystal Reflector. *Nano Lett.* **2015**, *15*, 4935−4941.

(27) Sutherland, B. R.; Hoogland, S.; Adachi, M. M.; Wong, C. T. O.; Sargent, E. H. Conformal Organohalide Perovskites Enable Lasing on Spherical Resonators. *ACS Nano* **2014**, *8*, 10947−10952.

(28) Li, J.; Si, J.; Gan, L.; Liu, Y.; Ye, Z.; He, H. Simple Approach to Improving the Amplified Spontaneous Emission Properties of Perovskite Films. *ACS Appl. Mater. Interfaces* **2016**, *8*, 32978−32983.

(29) Harwell, J. R.; Whitworth, G. L.; Turnbull, G. A.; Samuel, I. D. W. Green Perovskite Distributed Feedback Lasers. *Sci. Rep.* **2017**, *7*, 11727.

(30) Yakunin, S.; Protesescu, L.; Krieg, F.; Bodnarchuk, M. I.; Nedelcu, G.; Humer, M.; De Luca, G.; Fiebig, M.; Heiss, W.; Kovalenko, M. V.; et al. Low-Threshold Amplified Spontaneous Emission and Lasing From Colloidal Nanocrystals of Caesium Lead Halide Perovskites. *Nat. Commun.* **2015**, *6*, 8056.

(31) Papagiorgis, P.; Manoli, A.; Protesescu, L.; Achilleos, C.; Violaris, M.; Nicolaides, K.; Trypiniotis, T.; Bodnarchuk, M. I.; Kovalenko, M. V.; Othonos, A.; et al. Efficient Optical Amplification

in the Nanosecond Regime from Formamidinium Lead Iodide Nanocrystals. *ACS Photonics* **2018**, *5*, 907−917.

(32) Dey, A.; Rathod, P.; Kabra, D. Role of Localized States in Photoluminescence Dynamics of High Optical Gain CsPbBr$_3$ Nanocrystals. *Adv. Opt. Mater.* **2018**, *6*, 1800109.

(33) Veldhuis, S. A.; Tay, Y. K. E.; Bruno, A.; Dintakurti, S. S. H.; Bhaumik, S.; Muduli, S. K.; Li, M.; Mathews, N.; Sum, T. C.; Mhaisalkar, S. G. Benzyl Alcohol Treated CH$_3$NH$_3$PbBr$_3$ Nanocrystals Exhibiting High Luminescence, Stability, and Ultralow Amplified Spontaneous Emission Thresholds. *Nano Lett.* **2017**, *17*, 7424−7432.

(34) Chen, S.; Roh, K.; Lee, J.; Chong, W. K.; Lu, Y.; Mathews, N.; Sum, T. C.; Nurmikko, A. A Photonic Crystal Laser from Solution Based Organo-Lead Iodide Perovskite Thin Films. *ACS Nano* **2016**, *10*, 3959−3967.

(35) Qin, L.; Lv, L.; Li, C.; Zhu, L.; Cui, Q.; Hu, Y.; Lou, Z.; Teng, F.; Hou, Y. Temperature Dependent Amplified Spontaneous Emission of Vacuum Annealed Perovskite Films. *RSC Adv.* **2017**, *7*, 15911−15916.

(36) De Giorgi, M. L.; Perulli, A.; Yantara, N.; Boix, P. P.; Anni, M. Amplified Spontaneous Emission Properties of Solution Processed CsPbBr$_3$ Perovskite Thin Films. *J. Phys. Chem. C* **2017**, *121*, 14772−14778.

(37) Zhang, L.; Yuan, F.; Dong, H.; Jiao, B.; Zhang, W.; Hou, X.; Wang, S.; Gong, Q.; Wu, Z. One-Step Co-Evaporation of All-Inorganic Perovskite Thin Films with Room-Temperature Ultralow Amplified Spontaneous Emission Threshold and Air Stability. *ACS Appl. Mater. Interfaces* **2018**, *10*, 40661−40671.

(38) Pourdavoud, N.; Haeger, T.; Mayer, A.; Cegielski, P. J.; Giesecke, A. L.; Heiderhoff, R.; Olthof, S.; Zaefferer, S.; Shutsko, I.; Henkel, A.; et al. Room-Temperature Stimulated Emission and Lasing in Recrystallized Cesium Lead Bromide Perovskite Thin Films. *Adv. Mater.* **2019**, *31*, 1903717.

(39) De Giorgi, M. L.; Krieg, F.; Kovalenko, M. V.; Anni, M. Amplified Spontaneous Emission Threshold Reduction and Operational Stability Improvement in CsPbBr$_3$ Nanocrystals Films by Hydrophobic Functionalization of the Substrate. *Sci. Rep.* **2019**, *9*, 17964.

(40) Conings, B.; Drijkoningen, J.; Gauquelin, N.; Babayigit, A.; D'Haen, J.; D'Olieslaeger, L.; Ethirajan, A.; Verbeeck, J.; Manca, J.; Mosconi, E.; et al. Intrinsic Thermal Instability of Methylammonium Lead Trihalide Perovskite. *Adv. Energy Mater.* **2015**, *5*, 1500477.

(41) Gunasekaran, R. K.; Chinnadurai, D.; Selvaraj, A. R.; Rajendiran, R.; Senthil, K.; Prabakar, K. Revealing the Self-Degradation Mechanisms in Methylammonium Lead Iodide Perovskites in Dark and Vacuum. *ChemPhysChem* **2018**, *19*, 1507−1513.

(42) Li, J.; Wang, L.; Yuan, X.; Bo, B.; Li, H.; Zhao, J.; Gao, X. Ultraviolet Light Induced Degradation of Luminescence in CsPbBr$_3$ Perovskite Nanocrystals. *Mater. Res. Bull.* **2018**, *102*, 86−91.

(43) Quitsch, W.-A.; deQuilettes, D. W.; Pfingsten, O.; Schmitz, A.; Ognjanovic, S.; Jariwala, S.; Koch, S.; Winterer, M.; Ginger, D. S.; Bacher, G. The Role of Excitation Energy in Photobrightening and Photodegradation of Halide Perovskite Thin Films. *J. Phys. Chem. Lett.* **2018**, *9*, 2062−2069.

(44) Motti, S. G.; Gandini, M.; Barker, A. J.; Ball, J. M.; Srimath Kandada, A. R.; Petrozza, A. Photoinduced Emissive Trap States in Lead Halide Perovskite Semiconductors. *ACS Energy Letters* **2016**, *1*, 726−730.

(45) Barker, A. J.; Sadhanala, A.; Deschler, F.; Gandini, M.; Senanayak, S. P.; Pearce, P. M.; Mosconi, E.; Pearson, A. J.; Wu, Y.; Srimath Kandada, A. R.; Leijtens, T.; De Angelis, F.; Dutton, S. E.; Petrozza, A.; Friend, R. H. Defect-Assisted Photoinduced Halide Segregation in Mixed-Halide Perovskite Thin Films. *ACS Energy Letters* **2017**, *2*, 1416−1424.

(46) Huang, S.; Li, Z.; Wang, B.; Zhu, N.; Zhang, C.; Kong, L.; Zhang, Q.; Shan, A.; Li, L. Morphology Evolution and Degradation of CsPbBr$_3$ Nanocrystals under Blue Light-Emitting Diode Illumination. *ACS Appl. Mater. Interfaces* **2017**, *9*, 7249−7258.

(47) Li, Y.; Xu, X.; Wang, C.; Ecker, B.; Yang, J.; Huang, J.; Gao, Y. Light-Induced Degradation of CH$_3$NH$_3$PbI$_3$ Hybrid Perovskite Thin Film. *J. Phys. Chem. C* **2017**, *121*, 3904−3910.

(48) Christians, J. A.; Miranda Herrera, P. A.; Kamat, P. V. Transformation of the Excited State and Photovoltaic Efficiency of CH$_3$NH$_3$PbI$_3$ Perovskite upon Controlled Exposure to Humidified Air. *J. Am. Chem. Soc.* **2015**, *137*, 1530−1538.

(49) Aristidou, N.; Sanchez-Molina, I.; Chotchuangchutchaval, T.; Brown, M.; Martinez, L.; Rath, T.; Haque, S. A. The Role of Oxygen in the Degradation of Methylammonium Lead Trihalide Perovskite Photoactive Layers. *Angew. Chem., Int. Ed.* **2015**, *54*, 8208−8212.

(50) Li, X.; Ibrahim Dar, M.; Yi, C.; Luo, J.; Tschumi, M.; Zakeeruddin, S. M.; Nazeeruddin, M. K.; Han, H.; Gratzel, M. Improved Performance and Stability of Perovskite Solar Cells by Crystal Crosslinking with Alkylphosphonic Acid Omega-Ammonium Chlorides. *Nat. Chem.* **2015**, *7*, 703−711.

(51) Leo, K. Perovskite Photovoltaics: Signs of Stability. *Nat. Nanotechnol.* **2015**, *10*, 574−575.

(52) Juarez-Perez, E. J.; Ono, L. K.; Maeda, M.; Jiang, Y.; Hawash, Z.; Qi, Y. Photodecomposition and Thermal Decomposition in Methylammonium Halide Lead Perovskites and Inferred Design Principles to Increase Photovoltaic Device Stability. *J. Mater. Chem. A* **2018**, *6*, 9604−9612.

(53) Misra, R. K.; Aharon, S.; Li, B.; Mogilyansky, D.; Visoly-Fisher, I.; Etgar, L.; Katz, E. A. Temperature- and Component-Dependent Degradation of Perovskite Photovoltaic Materials under Concentrated Sunlight. *J. Phys. Chem. Lett.* **2015**, *6*, 326−330.

(54) Wang, Y.; Li, X.; Song, J.; Xiao, L.; Zeng, H.; Sun, H. All-Inorganic Colloidal Perovskite Quantum Dots: A New Class of Lasing Materials with Favorable Characteristics. *Adv. Mater.* **2015**, *27*, 7101−7108.

(55) Wang, Y.; Yu, D. J.; Wang, Z.; Li, X. M.; Chen, X. X.; Nalla, V.; Zeng, H. B.; Sun, H. D. Solution-Grown CsPbBr$_3$/Cs$_4$PbBr$_6$ Perovskite Nanocomposites: Toward Temperature-Insensitive Optical Gain. *Small* **2017**, *13*, 1701587.

(56) Yuan, F.; Wu, Z.; Dong, H.; Xi, J.; Xi, K.; Divitini, G.; Jiao, B.; Hou, X.; Wang, S.; Gong, Q. High Stability and Ultralow Threshold Amplified Spontaneous Emission from Formamidinium Lead Halide Perovskite Films. *J. Phys. Chem. C* **2017**, *121*, 15318−15325.

(57) Wang, S.; Yu, J.; Zhang, M.; Chen, D.; Li, C.; Chen, R.; Jia, G.; Rogach, A. L.; Yang, X. Stable, Strongly Emitting Cesium Lead Bromide Perovskite Nanorods with High Optical Gain Enabled by an Intermediate Monomer Reservoir Synthetic Strategy. *Nano Lett.* **2019**, *19*, 6315−6322.

(58) Brunetti, B.; Cavallo, C.; Ciccioli, A.; Gigli, G.; Latini, A. On the Thermal and Thermodynamic (In)Stability of Methylammonium Lead Halide Perovskites. *Sci. Rep.* **2016**, *6*, 31896.

(59) Aristidou, N.; Eames, C.; Sanchez-Molina, I.; Bu, X.; Kosco, J.; Islam, M. S.; Haque, S. A. Fast Oxygen Diffusion and Iodide Defects Mediate Oxygen-Induced Degradation of Perovskite Solar Cells. *Nat. Commun.* **2017**, *8*, 15218.

(60) Tian, Y.; Peter, M.; Unger, E.; Abdellah, M.; Zheng, K.; Pullerits, T.; Yartsev, A.; Sundström, V.; Scheblykin, I. G. Mechanistic Insights into Perovskite Photoluminescence Enhancement: Light Curing with Oxygen can Boost Yield Thousandfold. *Phys. Chem. Chem. Phys.* **2015**, *17*, 24978−24987.

(61) Brenes, R.; Guo, D.; Osherov, A.; Noel, N. K.; Eames, C.; Hutter, E. M.; Pathak, S. K.; Niroui, F.; Friend, R. H.; Islam, M. S.; et al. Metal Halide Perovskite Polycrystalline Films Exhibiting Properties of Single Crystals. *Joule* **2017**, *1*, 155−167.